INTERNATIONAL JOURNAL OF
COASTAL, OFFSHORE & ENVIRONMENTAL ENGINEERING IJCOE Vol..11/No.4 /Autumn 2026 (46-64)

Available online at: www. Ijcoe.org

Experimental and Numerical Investigation of the Effect of Stator and rotor distance on the Hydrodynamic Performance of a PumpJet Propulsion System

Mohammad Hossein Qaedsharaf [1]

[1] *Ph.D. in Mechanical Engineering, Khatam Al-Anbia Air Defense University, Tehran, Iran,* Mqaed1100@gmail.com

ARTICLE INFO

Article History:
Received: 31 July
Accepted: 10 Nov
Available online ….

Keywords:
pumpjet, Stator and rotor distance, Rotor diameter, Open-water efficiency, Thrust coefficient

ABSTRACT

This research investigates the effects of duct inlet length (L) and the distance between the rotor and stator on the hydrodynamic performance of a pre-swirl pump jet. For this aim, five geometries with different duct inlet lengths L equal to (0 ~ 0.1DRotor) were generated using a direct design method. Furthermore, these geometries were experimentally tested in a cavitation tunnel and validated through numerical simulations using ANSYS Fluent software; it can be concluded that there is good agreement between the experimental and numerical results. Additionally, uncertainty analysis was performed to control the accuracy of the experimental data. The results indicate that an increase in the duct inlet length and moving the stator closer to the rotor leads to more accurate guidance of exiting flow lines of the stator towards the rotor blades. This, in turn, increases the rotor lift coefficient and generates a greater pressure difference across the rotor, resulting in an increase in the total propulsor thrust coefficient and a subsequent rise in open-water efficiency at specific advance ratios. The maximum relative uncertainty for open-water efficiency was 1.79%. Among the tested configurations, the maximum open-water efficiency of 62.15% was observed for the L=0.1DR case at an advance ratio of 1.1. The minimum efficiency at the same advance ratio was 59.12% for the L=0DR case. Further analysis of the simulation results shows that the L=0.1DR case is superior to other configurations due to having the highest open-water efficiency (approximately 5% higher than the minimum value).

1- INTRODUCTION

The pre-swirl pumpjet mechanism is an advanced technology in marine propulsion that has garnered attention due to its capabilities in noise reduction and stealth, increased efficiency at high speeds, and improved performance compared to traditional propellers (Morrison, 2018; Suryanarayana et al., 2012). This system comprises a duct (flow-guiding tube), a stator (a set of fixed blades that pre-swirl the flow), and a rotor (rotating blades that generate thrust). The pre-swirl created by the stator can optimize the flow entering the rotor, thereby increasing system efficiency. One of the key aspects in designing this system is the consideration of geometric parameters, such as the duct inlet length and the stator-rotor gap. The duct inlet length, referring to the distance from the beginning of the duct to the stator, can affect flow development and uniformity before entering the stator. A longer duct inlet might stabilize the flow, but excessive length can lead to pressure drop and increased frictional losses. On the other hand, the stator-rotor gap, which indicates the distance between the trailing edge of the stator blades and the leading edge of the rotor blades, influences the interaction of the flow exiting the stator with the rotor. A tiny gap may cause undesirable flow interference, while a large gap can weaken the pre-swirl effect and reduce efficiency. The importance of these parameters lies in the fact that the hydrodynamic performance of a pre-swirl pumpjet system, including efficiency, thrust, torque, and cavitation behavior, is highly dependent on how the flow is managed (Renilson, 2018). This research proposes to investigate the effect of these two key parameters on hydrodynamic performance using a combination of experimental and numerical methods. In the experimental section, a scalable model of the pumpjet system will be designed and tested under controlled conditions to obtain data

such as thrust, torque, and flow patterns. In the numerical section, computational fluid dynamics (CFD) simulations using accurate turbulence models will be performed to provide more detailed insights into the flow, including complex interactions between the stator and rotor. This dual approach enables the cross-validation of data, yielding more reliable results. Additionally, uncertainty analysis will be used to verify the accuracy of the experiments. Uncertainty analysis and experimental design techniques emerged as a competitive approach in Western countries and Japan in the 1980s and 1990s (Dean & Voss, 1999). Uncertainty refers to determining the error range of a quantity, expressed with a 95% probability for engineering calculations (Nakra & Chaudhry, 2016; Coleman & Steele, 1999). It is evident that in uncertainty analysis, the goal is to determine the contribution of each parameter's error to the total quantity error. Therefore, experimental data and tests are required. The significance of this research extends beyond immediate applications in marine propulsion. A better understanding of flow interactions in ducted systems with stators and rotors can also aid in the design of hydroelectric turbines or other fluid turbomachinery. Ultimately, this research aims to fill existing knowledge gaps, provide comprehensive experimental and numerical data, and develop guidelines for designing pre-swirl pumpjet systems. The results of this study are expected not only to contribute to a better understanding of the hydrodynamic behavior of these systems but also to lead to the development of technologies that will improve the performance and efficiency of future vessels. Pumpjets come in various types depending on the rotor and stator arrangement. The pre-swirl pumpjet is a type where the stator is positioned at the flow inlet into the duct. This type of pumpjet has gained attention due to its low noise levels. A pumpjet system consists of a rotor, a stator, a duct, a hub, and a nose. Fig. 1 shows a schematic of the components of a stator-rotor pumpjet.

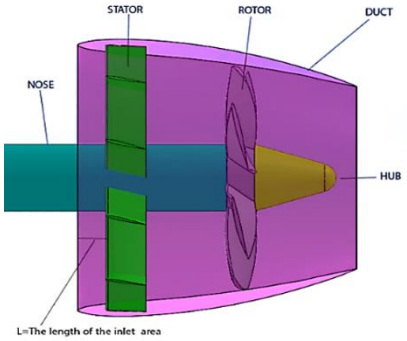


Fig. 1 Schematic of Pre-swirl Pumpjet Components

2- BACKGROUND RESEARCH AND STUDIES

A summary of key studies relevant to the topic is presented below: Qaedsharaf et al. (2025) numerically investigated the cavitating performance of a pre-swirl pump-jet propulsion system by varying the chord length of the stator airfoil. Their findings indicate that increasing the stator chord length up to a certain point improves the propulsor's cavitating performance and reduces the likelihood of cavitation. Li et al. (2022) examined the hydrodynamic performance of a submarine equipped with a novel pump-jet propulsor. Their study noted that duct and stator configurations influence performance, though specific details regarding the inlet length or spacing were limited. Weng et al. (2024) investigated the hydrodynamic noise characteristics of a pump-jet through both numerical and experimental methods. The results show that the amplitude of sound pressure level fluctuation in the radial plane exhibits an approximately circular distribution, and the sound pressure level also possesses characteristics of a dipole source. Zou et al. (2024) explored the relationship between longitudinal vibration size, frequency changes, excitation force, and the effect of vibration magnitude on the excitation force and vortex dynamic characteristics of a pump-jet propulsor. Ji et al. (2024) investigated the effect of rotor blade tip rake angle on the excitation force of a pump-jet propulsor in the same year. Their results demonstrate that the oscillation amplitude of the resulting horizontal (and vertical) forces acting on the duct/stator assembly significantly decreases with a reduced rake angle and increases with its increment. Weng et al. (2024) examined a pumpjet's hydrodynamic and noise performance with different stator pre-swirl angles. Utilizing the SBES method and Lighthill's acoustic analogy, they found that pre-swirl angles modulate pressure fluctuations and noise, which is indirectly related to changes in ambient pressure. Zhou et al. (2023) numerically analyzed the effects of duct profile parameters, such as camber and angle of attack, on the flow characteristics of a pump jet. They found these parameters affect flow uniformity and efficiency, indirectly linking to the duct inlet conditions. However, this study did not specifically investigate inlet length or consider uncertainty analysis. Kim et al. (2023) performed a parametric study on the hydrodynamic characteristics of a pumpjet installed on a SUBOFF submarine. They investigated the influence of duct incidence and stator twist angles and reported that the duct increases internal pressure, but the analysis was limited to a constant depth. Bi et al. (2023) explored the effect of rotor tip grooves on cavitation and the hydrodynamic performance of a pumpjet. Using CFD, they showed that grooves can reduce tip cavitation, but the study was conducted

under constant pressure conditions. Zhou et al. (2022) comprehensively reviewed pump-jet hydrodynamic performance and design. They highlighted the importance of duct design in improving efficiency and reducing noise but did not address the duct inlet length. This study also did not mention uncertainty analysis, indicating a need for more rigorous approaches in future research. Huang et al. (2022) investigated the evolution of wake vortices and unsteady forces in a pre-swirl pumpjet. Through DES simulations, they demonstrated that stator-rotor interaction complicates the internal flow, but the effect of depth variations was not explored. Ye et al. (2022) investigated tip flow control performance in a pumpjet, analyzing the effect of axial slots on cavitation and efficiency using the DES method. This study did not address depth variations. Zhao et al. (2022) examined the cavitation-vortex interaction in a pre-swirl pumpjet using the DES method and a homogeneous cavitation model. They reported that heavy cavitation (σ=2.2) reduces hydrodynamic loading and accelerates vortex collapse. This study was conducted at a constant depth and did not consider depth variations. Lidtke et al. (2022) investigated cavitation-induced noise in propellers and demonstrated that ambient pressure influences noise intensity. This analysis is relevant for understanding the effects of depth in pump jets. The findings are beneficial for stealth applications. Sun et al. (2022) compared the hydrodynamic performance of pre-stator and post-stator pumpjets under cavitating conditions. Employing the DES method, they showed that stator-rotor interaction affects efficiency and cavitation, but their analysis was limited to constant depth conditions. Chen et al. (2021) combined CFD and experimental methods to investigate the effect of duct inlet length on the hydraulic performance of a waterjet propulsion device. They found that duct efficiency, head, and thrust peaked at an optimal length (L=1.12D), and flow uniformity improved with increasing length. Although this study focused on water jets, its findings are generalizable to pump jets; however, the absence of uncertainty analysis limited the accuracy of the results. Huang et al. (2021) used advanced DES simulation to investigate the effects of duct parameters on the unsteady hydrodynamic performance of a pump jet. They showed that duct geometry influences thrust fluctuations and noise, but the duct inlet length was not explicitly examined. Qiu et al. (2020) investigated a pumpjet's hydrodynamic and cavitation performance under oblique flow conditions with varying tip clearances. Using a RANS model and the Zwart-Gerber-Belamri cavitation model, it was demonstrated that tip cavitation on the rotor is exacerbated under oblique flow, which could be linked to changes in ambient pressure. This research did not address variations in depth but emphasized the significance of flow conditions. Qiu et al. (2022) investigated cavitation performance at various cavitation numbers (ranging from 1.4721 to 7.5682). Their study revealed that a lower cavitation number (1.4721) reduced efficiency by up to 37%. This analysis is directly relevant to ambient pressure variations caused by depth. Applying a hybrid CNN-Bi-LSTM model for force prediction offers an innovative approach. Wang et al. (2020) examined the influence of duct geometric parameters on the hydrodynamic performance of a pump jet using a surface panel method. They analyzed parameters such as gap size, camber, and angle of attack, finding that these factors affect performance indicators, surface pressure distribution, and flow velocity. However, this study did not specifically address the duct inlet length or consider uncertainty analysis, indicating a need for more focused research. This study also did not include uncertainty analysis, which limits its ability to provide reliable results. Using uncertainty analysis, Qaedsharaf et al. (2019) compared the performance and sensitivity of influential parameters in two propellants, oxygenated water and nitrous oxide. The results showed that using nitrous oxide propellant would be more desirable in accuracy, and its propulsive force would be closer to the desired propulsive force of 5 Newtons. Motallebi-Nejad et al. (2017), though slightly older, is relevant due to its use of uncertainty analysis in CFD simulations for ducted propellers and pump jets. They employed the Grid Convergence Index (GCI) method to evaluate numerical errors, providing a framework for the present study. However, this study also did not address the duct inlet length. Qaedsharaf (2011), in his Master's thesis on heat transfer analysis and regression rate of solid fuel hybrid propellants using uncertainty analysis and curve fitting, obtained an empirical relationship for the heat transfer rate of hybrid propellants.

2-1 Research Gaps

Despite these advancements, several gaps persist in the scientific literature: Combined Effects of Parameters: Most studies focus on either duct geometry or stator parameters in isolation. There is a lack of systematic research investigating the combined effects of duct inlet length and stator-rotor clearance, especially in pre-swirl pump jets. Experimental Validation: Many studies rely on numerical simulations with limited experimental validation. Comprehensive experimental data is needed to confirm CFD results and ensure applicability in real-world conditions. Specific Focus on Pre-swirl Pump-jet Propulsion: Although pre-swirl pump-jets have been explored in some studies, the unique flow dynamics resulting from pre-swirl have not consistently been the central focus of the investigation, which is crucial for translating research findings into practical designs. Lack of Uncertainty Analysis: The use of uncertainty analysis in experimental pump-jet tests is minimal, which can reduce the accuracy and reliability of results.

2-2 Relation to Previous Studies and Significance of the Topic

The present study builds upon previous research to address the identified gaps. It combines insights from studies such as Weng et al. (2024) and Zhou et al. (2023) regarding duct geometry with findings from Li et al. (2022) concerning stator-rotor interactions. By systematically varying both duct inlet length and stator-rotor clearance, this research aims to provide a comprehensive understanding of their effect on hydrodynamic performance, including efficiency and thrust parameters. The simultaneous use of experimental and numerical methods ensures robust validation, addressing the limitation of simulation-based studies. With a specific focus on pre-swirl pump jets, this study targets a critical subset of propulsion systems with unique flow dynamics. The findings of this research can contribute to the design of more efficient submerged vessels, aiding in operational stability and effectiveness in marine applications.

3- RESEARCH METHODOLOGY

3-1 Geometry Extraction

The geometry design of the pumpjet propulsion system model is based on maximizing hydrodynamic performance using the direct design method (Zhou et al., 2022).

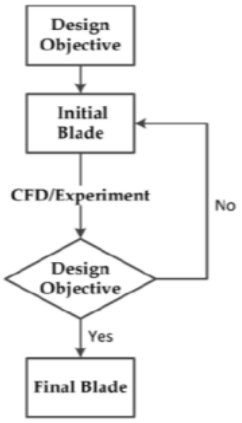


Fig. 2 Direct Design Algorithm (Zhou et al., 2022)

Table 1 shows the geometric specifications of the designed propulsion system, and Fig. 3 shows its general schematic.

Table 1. Geometric specifications of the pump jet propulsion system

Characteristic	Value
Rotor diameter (cm)	9
Number of rotor blades and their profile	7 - NACA16
Number of stator blades and their profile	11 - NACA66
Duct type and its profile	Convergent - NACA6608
Inlet diameter, outlet diameter and duct length (cm)	13.06, 9.12, and 12.05

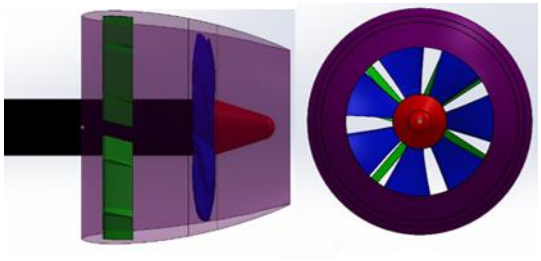


Fig. 3 Schematic of the geometry designed by the direct design method

To investigate the effect of the duct inlet area and the distance between the rotor and stator on the hydrodynamic performance of the propulsion system, five models were designed by displacing the stator from the duct inlet towards the rotor. These models had inlet lengths (L) of 0 DR, 0.025 DR, 0.050 DR, 0.075 DR, and 0.1 DR (DR: Rotor Diameter), and numerical simulations were performed on each model separately. It should be noted that during the geometry generation process, the optimal duct length was determined, and the stator was displaced at this optimal length, starting from the duct inlet towards the rotor. A schematic of the rotor and stator positions in the designed geometries is presented in Fig. 4.

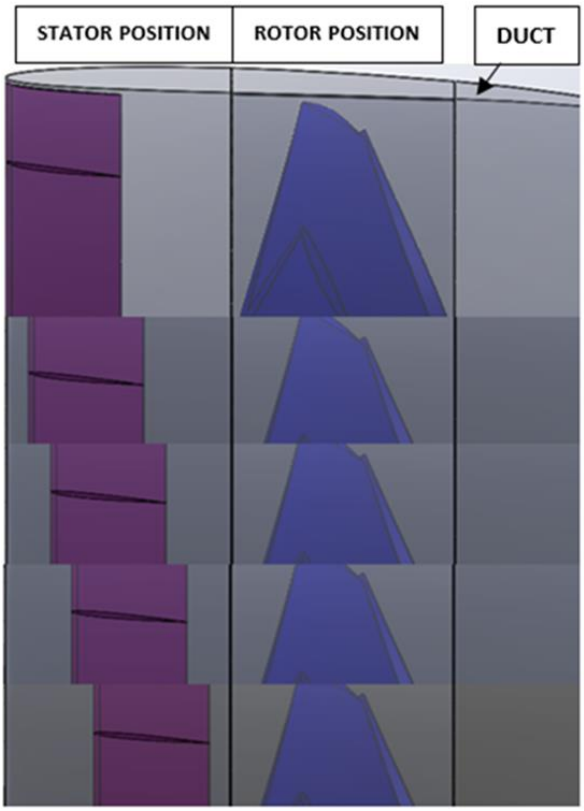


Fig. 4 Schematic of rotor and stator positions for designed geometries with inlet zone lengths of 0, 0.025, 0.05, 0.075, and 0.1 rotor diameters, from top to bottom, respectively

4- EXPERIMENTAL TEST

The experimental test was conducted inside the cavitation tunnel of Imam Khomeini Naval University in Nowshahr. The cavitation tunnel is a NA10 model manufactured in England. The tunnel specifications are presented in Table 2. A view of the tunnel is also visible in in Fig. 5.

Table 2. Cavitation tunnel specifications

Characteristic	Value
Tunnel dimensions (mm)	1100*2750*4900
Test section dimensions (mm)	750*200*200
Flow velocity range (m/s)	0.65~4.8
Maximum impeller rotational speed (rpm)	3000
Adjustable pressure range (Kpa)	50~200



Fig. 5 View of Nowshahr Naval University's Cavitation Tunnel

To install the geometry inside the cavitation tunnel, an airfoil-shaped strut was embedded below the designed geometries, along with a tab for measuring the thrust force of the duct and stator assembly via a load cell. The geometries were fabricated with a 3D printer using composite materials with 1-micron precision. A schematic of the five manufactured geometries is shown in Fig.6.



Fig. 6 Five geometries manufactured for experimental testing

The load cell and propeller holding mechanism were secured in the tunnel with three weights. The rotor was also separately installed on the drive shaft, which was connected to the thrust and torque measurement equipment. A schematic of the propeller installation is shown in Fig. 7. Fig. 8 shows an image of the propeller in operation.

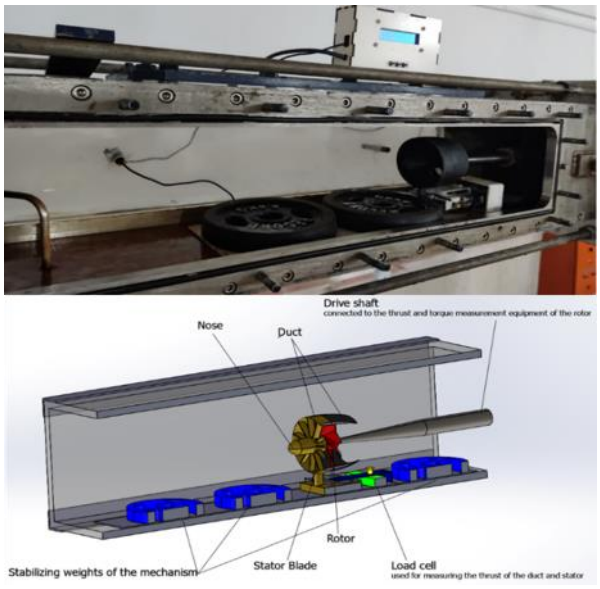


Fig. 7 Schematic of thruster installation within the tunnel

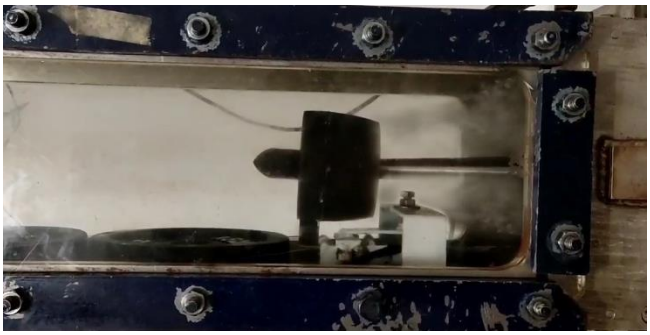


Fig. 8 Propeller installed inside the tunnel operating. The three measurable parameters are rotor thrust, duct and stator thrust, and rotor torque.

Subsequently, 8 advance ratios were considered, and for each advance ratio, each of these 3 parameters was measured 4 times, and their average was used in the relationships. Data collection was performed at 25 degrees Celsius, sea level pressure (101 kPa), and water with a density of 1000 kg per cubic meter. n has a constant value of 27.8 revolutions per second, and VA is adjusted according to the advance ratio by tunnel equipment that has been previously calibrated and approved by a qualified company. To re-verify the adjusted flow speed, it was compared with the speed set by electronic speed control equipment using a Pitot tube installed inside the test section, which confirmed its accuracy.

5- PUMPJET FUNCTIONAL PARAMETERS

To investigate the hydrodynamic performance of a pumpjet propulsion system, the following dimensionless coefficients are defined (Carlton, 2012; Bertram, 2012)
:

$$\begin{cases} J = \frac{V_A}{nD} \quad K_{TR} = \frac{T_R}{\rho n^2 D^4} \quad K_{TS} = \frac{T_s}{\rho n^2 D^4} \quad K_{TD} = \frac{T_D}{\rho n^2 D^4} \\ K_{QR} = \frac{Q_R}{\rho n^2 D^5} \quad K_Q = K_{QR} \quad K_T = K_{TR} + K_{TS} + K_{TD} \\ \eta_o = \frac{JK_T}{2\pi K_Q} \end{cases} \quad (1)$$

Where J is advance ratio, K_T is total thrust coefficient, K_{TR} is rotor thrust coefficient, K_{TS} is stator thrust coefficient, K_{TD} is duct thrust coefficient, K_Q is torque coefficient, K_{QR} is rotor torque coefficient, η_o is open-water propeller efficiency, D is propeller diameter (m), n is rotational speed (rps), V_A is advance velocity (m/s), ρ is water density(kg/m^3).

6- UNCERTAINTY EQUATIONS

If we calculate the open water efficiencyη_o from the above relationships, we will have:

$$\eta_o = \frac{JK_T}{2\pi K_Q} = \frac{V_A(T_R + T_D + T_S)}{2\pi nQ} = \frac{V_A T_{Tot}}{2\pi nQ} \quad (2)$$

The total thrust is the sum of the rotor, duct, and stator thrusts. In the conducted experimental test, the thrust of the duct and stator assembly was sampled multiple times together, while the rotor thrust and torque were sampled separately. These values are then substituted into the relationships after averaging multiple sampling instances. Let's assume the quantity η_o is the primary quantity, which is a function of the independent parameter J:

$$\eta_o = f(X_1.X_2.\dots X_J) = f(V_A.T_{Tot}.n.Q) \quad (3)$$

Accordingly, the reduced equation will be:

$$\eta_o = \frac{V_A T_{Tot}}{2\pi nQ} \quad (4)$$

The sensitivity of η_o to the results of each of these parameters is then obtained by substituting the results into the following relationship (Nakra & Chaudhry, 2016):

$$Sensitivity = \left(\frac{\partial \eta_o}{\partial X_i}\right) \quad (5)$$

The uncertainty of η_o arises from the uncertainty of the effective input values (x_i) on the governing equation, or the error of each parameter (U_{X_i}) (Nakra & Chaudhry, 2016):

$$U_{\eta_o} = \sqrt{\sum_{i=1}^{n} \left(\frac{\partial \eta_o}{\partial X_i} U_{X_i}\right)^2} \quad ; U - U_{\eta_o} \le U_t \le U + U_{\eta_o} \quad (6)$$

In the error analysis process, after determining the uncertainty value of each parameter (U_X), which is obtained from measurements, and by using statistical relationships and sensitivity analysis of the governing equation, the amount of uncertainty in the primary quantity (U_{η_o}) is determined. It can then be stated that the true value (U_t) lies within the obtained range. The smaller the value of Uηo, the higher the certainty in the quantity η_o (the obtained range will be smaller), and it approaches a more reliable value. It can be concluded that the total uncertainty results from the uncertainty in each parameter, and by reducing the uncertainty in the parameters, the certainty in the value of that quantity can be increased. Therefore, the uncertainty for the function η_o represents the dependency of the function η_o on parameter x and the error present in that parameter (RSS) (Nakra & Chaudhry, 2016):

$$U_{\eta_o}^2 = \left(\frac{\partial \eta_o}{\partial X_1}\right)^2 U_{X_1}^2 + \left(\frac{\partial \eta_o}{\partial X_2}\right)^2 U_{X_2}^2 + \dots + \left(\frac{\partial \eta_o}{\partial X_J}\right)^2 U_{X_J}^2 \quad (7)$$

Now, if the relative uncertainty is considered (Nakra & Chaudhry, 2016):

$$\frac{U_{\eta_o}^2}{\eta_o^2} = \left(\frac{X_1}{\eta_o}\frac{\partial \eta_o}{\partial X_1}\right)^2 \left(\frac{U_{X_1}}{X_1}\right)^2 + \left(\frac{X_2}{\eta_o}\frac{\partial \eta_o}{\partial X_2}\right)^2 \left(\frac{U_{X_2}}{X_2}\right)^2 + \dots + \left(\frac{X_J}{\eta_o}\frac{\partial \eta_o}{\partial X_J}\right)^2 \left(\frac{U_{X_J}}{X_J}\right)^2 \quad (8)$$

In the latter relationship, other parameters can be replaced with the open water efficiency. Relative uncertainty is often expressed as a percentage. The measurable parameters in the conducted experimental test include: rotor thrust, rotor torque, and the thrust of the duct and stator assembly. The value of n is a constant 27.8 revolutions per second, and V_A is adjusted depending on the advance ratio via tunnel equipment, which has been previously calibrated and verified by a qualified company. To calculate the values of total uncertainty, relative uncertainty, and sensitivity analysis, relevant relationships were programmed in MATLAB software, and the corresponding results were extracted.

7- NUMERICAL SIMULATION APPROACH

Numerical simulation approach: In this study, the working fluid is considered incompressible, homogeneous, and Newtonian. Body forces, gravitational acceleration, and heat transfer are

neglected. The fluid flow is calculated by the Navier-Stokes equations, which are very time-consuming and almost impossible to solve analytically. Using the Reynolds averaging method for 5 equations is a common approach for solving viscous flow and Navier-Stokes equations. This approach introduces Reynolds stresses that need to be solved. Turbulence models, by introducing a turbulent viscosity, calculate Reynolds stresses. In this study, the k-ω SST turbulence model was used. Among the two-equation models, the k-ω model has several advantages over the k-ε model. Its most prominent advantage is that it can be integrated without additional components in the viscous sublayer. This makes the behavior of y+ insensitive and straightforward. Moreover, the k-ω SST model performs better in predicting separation and unwanted pressure gradients. Considering the effects of boundary layer growth on the hydrodynamic performance of the pump jet, k-ω may be preferred over k-ε [31]. One of the disadvantages of the standard k-ω equation is the high sensitivity of the solution to the value of free stream k and ω outside the shear layer. For this reason, the use of the standard k-ω model in ANSYS Fluent software is not recommended. The k-ω BSL and k-ω SST models are designed by combining components of the ω and ε equations to avoid sensitivity to the free stream in the standard k-ω model. Also, the k-ω SST model is well calibrated for accurately calculating separation from smooth surfaces. Among the k-ω models, it is recommended to use the SST or BSL model (Bertram, 2012; Qin et al., 2021; Yang et al., 2022). Since the Reynolds numbers on both sides of the pump jet duct are different, there is a significant region of laminar flow outside the duct, especially at low advance ratios. The difference in flow regimes affects the duct thrust. According to the studies conducted, when there is a significant difference in the Reynolds numbers on both sides of the duct and the outer passage has a Reynolds number less than the minimum Reynolds number accepted by ITTC (5*10^5) when the advance speed is low, the effect of the difference in flow regimes on the duct thrust is negligible because the duct thrust is affected by its pressure component and its friction component will be very small. Therefore, the transition on the duct was neglected in this study.

7-1 Main Governing Equations

For an incompressible and single-phase fluid, the governing equations for URANS can be written in tensor form as the conservation of mass and momentum (Li et al., 2022):

$$\frac{\partial \rho U_i}{\partial x_i} = 0 \tag{9}$$

$$\frac{\partial(\rho U_i)}{\partial t} + \frac{\partial(\rho U_i U_j)}{\partial x_j} = -\frac{\partial P}{\partial x_i} + \frac{\partial}{\partial xj}\left[\mu\left(\frac{\partial Ui}{\partial x_j} + \frac{\partial Uj}{\partial x_i}\right)\right] + \frac{\partial}{\partial xj}(-\rho\overline{u_\iota u}j) + S_M \tag{10}$$

Where i=1,2,3, j=1,2,3, ρ is the fluid density and x_i, xj are Cartesian coordinate components. For a fixed coordinate system, S_M is equal to zero, and Ui and Uj represent the components of the absolute velocity. For a moving reference frame, S_M is the sum of the Coriolis component and the component of the centrifugal forces ω×(r×ω), and Ui, Uj are the components of the relative velocity. μ is the dynamic viscosity, P is the pressure, and $\rho\overline{u_\iota u}j$ represents the Reynolds stresses.

7-2 Boundary Conditions and Numerical Simulation Settings

The entire computational domain is divided into two subdomains: the rotor domain and the outer domain. The outer domain has a section similar to a cavitation tunnel with a length of 15D. The rotor is located 5D from the inlet. All subdomains have an unstructured mesh. Near the walls, the height of the first layers of the boundary layer sublayers is calculated with a y+ value in the range of ٠ to °, which is suitable for the RANS solver with the SST k-w turbulence model. The boundary conditions are also shown in Fig. 9. A uniform upstream flow with a velocity V corresponding to the advance ratio J and a turbulence intensity of 1% is set at the inlet boundary. A pressure outlet boundary condition with a constant pressure Pout equal to 1 atm is applied to the outlet. The far-field wall is set as a wall with zero shear stress. During the simulation, the rotational speed of the rotor, n, was kept constant at 27.8 revolutions per second, while the inlet velocity varied depending on the advance ratio. All simulations were performed using ANSYS Fluent software with the SIMPLEC algorithm, second-order discretization for momentum, and PRESTO discretization for pressure. A total of 3000-time steps with 20 iterations per time step were used until convergence (minimum residual of 1*10^-6) was achieved. The time step was calculated using the equation Δt=1/(360n), where n is the rotational speed in revolutions per second. The working fluid is water at 20 degrees Celsius, with a density of 1000 kg/m^3 and a saturated vapor pressure of 2368 Pascals. Since temperature changes underwater are negligible, temperature variations are ignored, water properties are considered constant, and the water is assumed to be free of physical contamination. The quality of each computational subdomain is greater than 0.5.

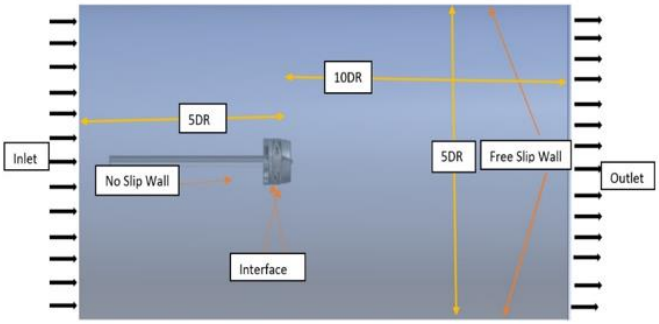


Fig. 9 Boundary conditions used in the numerical simulation

8- GRID INDEPENDENCE STUDY

In any numerical simulation, it is essential to ensure that the results are independent of the number and type of computational cells used. The grid convergence index (GCI) method, first proposed by Roache (Roache, 1997), is used to assess the discretization error and numerical uncertainties. This method requires at least three grids with different numbers of cells: S1, S2, and S3, with N1, N2, and N3 elements, respectively, from the finest (1) to the coarsest (3) grid. The grid refinement factor (r) is defined as:

$$r_{21} = (\frac{N1}{N2})^{1/3} \quad (11)$$

If r > √3, the extrapolation error decreases (Roache, 1997).

According to Roache's method, the convergence ratio is defined as:

$$R=\frac{\varepsilon_{21}}{\varepsilon_{32}}=\frac{\eta_2-\eta_1}{\eta_3-\eta_2} \quad (12)$$

where η_1 ،η_2 and η_3 are the open-water efficiency for the three cases. In this equation ε_{ij}, represents the difference in results obtained from solving using the i,j grid. For the convergence ratio, three scenarios can be considered:

- If R > 1, the grid is diverging.
- If R < 0, the convergence is oscillatory.
- If 0 < R < 1, the grid is converging monotonically.

When the solutions obtained with the investigated grids are in a converged state, Richardson extrapolation is used to estimate the order of convergence. The order of accuracy of this algorithm is calculated according to equation (11), where r is the grid refinement ratio, as defined earlier (Roache, 1997):

$$P=\frac{\ln(\frac{\varepsilon_{32}}{\varepsilon_{21}})}{\ln(r)}=\frac{\ln(\frac{\eta_3-\eta_2}{\eta_2-\eta_1})}{\ln(r)} \quad (13)$$

Finally, the grid convergence index is calculated using equation (12). In this equation, the factor Fs is the convergence assurance factor, and a value of Fs=1.25 is recommended (Roache, 1997). Additionally, in this equation, the symbol $|\varepsilon_{ij}|$ represents the approximate relative error.

$$\begin{cases} GCI_{fine} = F_s\frac{|\varepsilon_{12}|}{r^p-1}=\frac{F_s}{(r^p-1)}\left|\frac{\eta_1-\eta_2}{\eta_1}\right. \\ GCI_{coarse} = F_s r^p\frac{|\varepsilon_{23}|}{r^p-1}=\frac{F_s r^p}{(r^p-1)}\left|\frac{\eta_2-}{\eta_2}\right. \end{cases} \quad (14)$$

The grid convergence index indicates how far the obtained results are from the exact value. In other words, this method shows how the results change as the grid is refined. Small values of this index indicate that further refinement of the grid will not improve the results. Grid networks are reconstructed by decreasing and increasing the first layer height. Based on a Y+ value of ٭, the first layer thickness is calculated as 0.0045 mm (for a fine mesh). For grid independence analysis, values of 0.0050 mm and 0.0055 mm are chosen as the medium and coarse settings, respectively. Numerical simulations were performed at two different Courant numbers, 0.8 and 0.9, for fine, medium, and coarse meshes, with the results shown in Table 3.

Table 3. Grid independence study for thrust and torque coefficients at different advance ratios

Advance ratio	*First Layer Height*	*number of cells (million)*	K_T	K_Q
J=0.8	$\Delta s_1 = 0.0055$	N_1 =12.2	K_{T1} = 0.3502	K_{Q1} =0.0817
	$\Delta s_2 = 0.0050$	N_2 =15.6	K_{T2} =0.3476	K_{Q2} =0.0808
	$\Delta s_3 = 0.0045$	N_3 =20.5	K_{T3} =0.3470	K_{Q3} =0.0801
J=0.9	$\Delta s_1 = 0.0055$	N_1 =12.2	K_{T1} =0.3140	K_{Q1} =0.0773
	$\Delta s_2 = 0.0050$	N_2 =15.6	K_{T2} =0.3119	K_{Q2} =0.0766
	$\Delta s_3 = 0.0045$	N_3 =20.5	K_{T3} =0.3111	K_{Q3} =0.0762

As shown in Table 3, the errors of thrust and torque coefficients are very low among the three mesh types, confirming the grid independence. Additionally, the Grid Convergence Index (GCI) was calculated. The efficiencies of the three defined grids at J=0.9 are 3501.60, 3522.58, and 3567.58, respectively. Also, GCIfine and GCIcoarse are 0.0111 and 0.0113, respectively, which are small and desirable values. The convergence ratio R is 1.002, a value close to 1, indicating grid convergence. Therefore, Δs2=0.0050 was selected for meshing in all cases. The Meshed geometry is visible in Fig. 10.



Fig. 10 Meshed geometry

9- DISCUSSION OF RESULTS

9-1 Case 1: L=0DR

In this case, the inlet section length is considered 0, and the stator is positioned at the duct's inlet. Based on the

average of 4 samples of thrust and torque values from the experimental test, the maximum efficiency is ٥٩,١٢% at an advance ratio of 1.1. The maximum thrust coefficient is 0.4765, and the maximum torque coefficient is 0.09651. The thrust coefficient exhibits a nearly linear decreasing trend as the advance ratio increases. The open-water efficiency plot exhibits a completely ascending trend up to J = 1.1 and a completely descending trend thereafter. The thrust and torque coefficient plots exhibit a decreasing trend with an increasing advance ratio, except for minor fluctuations. The plots of efficiency, thrust, and torque coefficients at various advance ratios are presented in Fig. 11,12.

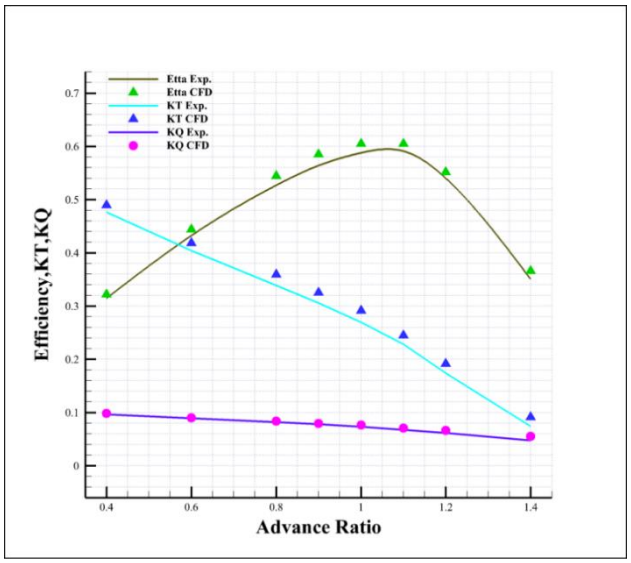


Fig. 11 Open-water efficiency, thrust, and torque coefficients at various advance ratios for the L=0DR case.

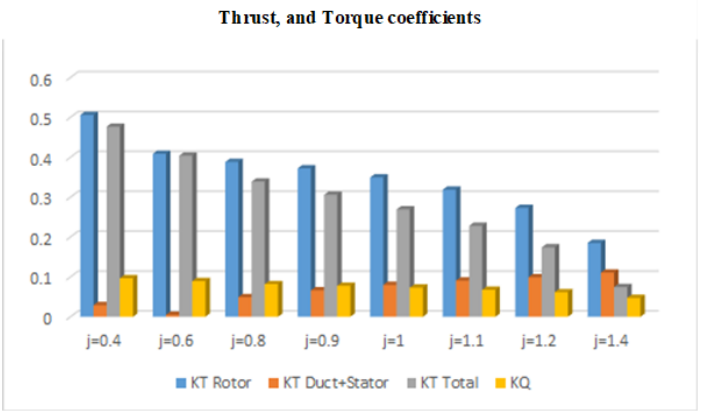


Fig. 12 Bar chart of rotor thrust coefficient, duct+stator thrust coefficient, total thrust coefficient, and torque coefficient obtained from experimental test results for the L=0DR case.

As observed from the results in Fig. 11, there is good agreement between the experimental test results and numerical simulations. Fig. 12 also presents the thrust and torque coefficients as bar charts, calculated using the average measured values of rotor thrust, duct-stator thrust, total thrust, and rotor torque. Fig. 13 shows the relative uncertainty values (in percent) for duct-stator thrust, rotor thrust, total thrust, rotor torque, and open-water efficiency. As indicated by the graph, the maximum relative uncertainty occurs for open-water efficiency at 1.784863%, which is less than 5%, indicating the high accuracy of the conducted experiments.

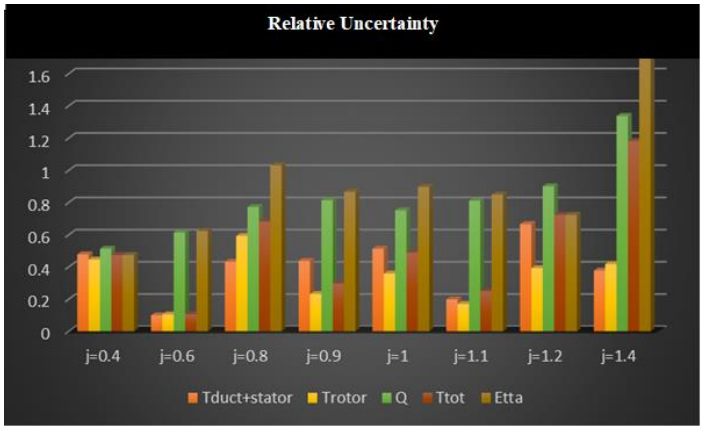


Fig. 13 Relative uncertainty values (in percent) for duct-stator thrust, rotor thrust, total thrust, rotor torque, and open-water efficiency at various advance ratios for the L=0DR case.

9-2 Case 2: L=0.025DR

In this case, the inlet section length is considered to be 0.0٠225 meters. Based on the average of 4 sets of sampled thrust and torque values from the experimental test at different advance ratios, the maximum open-water efficiency is 51.59% at an advance ratio of 1.1. The maximum thrust coefficient is 0.4887, and the maximum torque coefficient is 0.09723. Similar to the previous case, the open-water efficiency curve shows a completely ascending trend up to J=1.1 and then a completely descending trend beyond this advance ratio. The thrust coefficient and torque coefficient curves generally show a decreasing trend with increasing advance ratio, apart from minor fluctuations. Fig. 14 presents the efficiency, torque, and thrust coefficient values at various advance ratios. As the results indicate, there is good agreement between the experimental test results and numerical simulations. Fig. 15 also shows the thrust and torque coefficients as bar charts, calculated using the average measured values of rotor thrust, duct-stator thrust, total thrust, and rotor torque. Fig. 16 presents the relative uncertainty values of duct-stator thrust, rotor thrust, total thrust, rotor torque, and open-water efficiency as percentages. As the graph shows, the maximum relative uncertainty occurs for open-water efficiency at 1.689285%, which is less than 5%, indicating the high accuracy of the experiments.

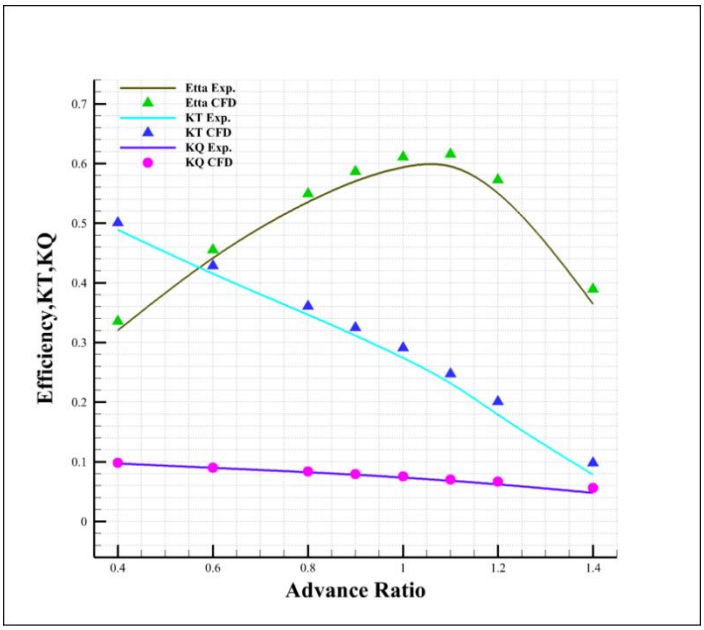


Fig. 14 Open-water efficiency, thrust, and torque coefficients at various advance ratios for L=0.025DR

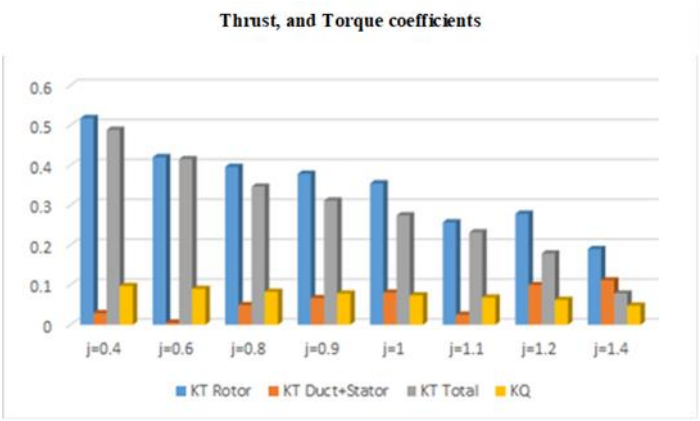
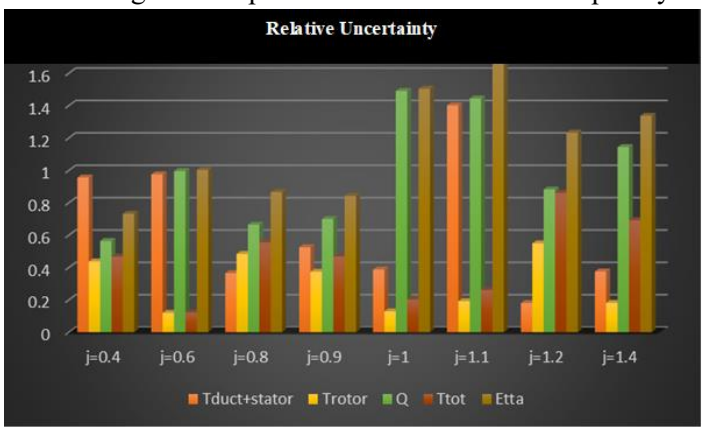


Fig. 15 Bar chart of rotor thrust coefficient, duct+stator thrust coefficient, total thrust coefficient, and torque coefficient obtained from experimental test results for L=0.025DR

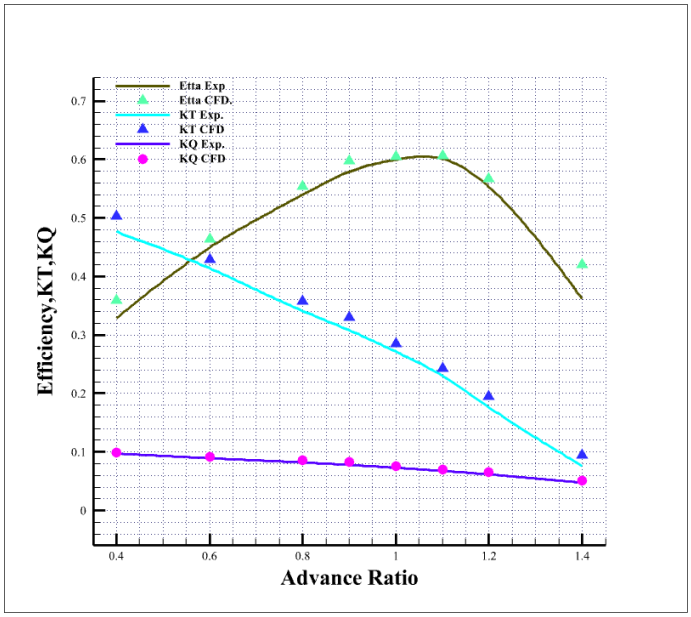
Fig. 16 Relative uncertainty values of duct-stator thrust, rotor thrust, total thrust, rotor torque, and open-water efficiency parameters as percentages at various advance ratios for L=0.025DR

9-3 Case 3: L=0.050DR

In this case, the duct inlet section length is considered to be 0.045 meters. Based on the average of 4 sets of sampled thrust and torque values from the experimental test at different advance ratios, the maximum efficiency is 60.09% at an advance ratio of 1.1. The maximum thrust coefficient is 0.5019, and the maximum torque coefficient is 0.0973. Similar to the previous case, the open-water efficiency curve shows a completely ascending trend up to J=1.1 and then a completely



descending trend beyond this advance ratio. As in the



previous case, there are no significant oscillatory peaks in the thrust and torque coefficient curves, and a decreasing trend is observed, with good agreement between the experimental test results and numerical simulations. Fig. 17 presents the efficiency, torque, and thrust coefficient values at various advance ratios. Fig. 18 also shows the thrust and torque coefficients as bar charts, calculated using the average measured values of rotor thrust, duct-stator thrust, total thrust, and rotor

torque. Fig. 19 presents the relative uncertainty values of duct-stator thrust, rotor thrust, total thrust, rotor torque, and open-water efficiency as percentages. As the graph shows, the maximum relative uncertainty occurs for open-water efficiency at 1.794044%, which is less than 5%, indicating the high accuracy of the experiments.

Fig. 17 Efficiency, thrust, and torque coefficients at various advance ratios for L=0.050DR

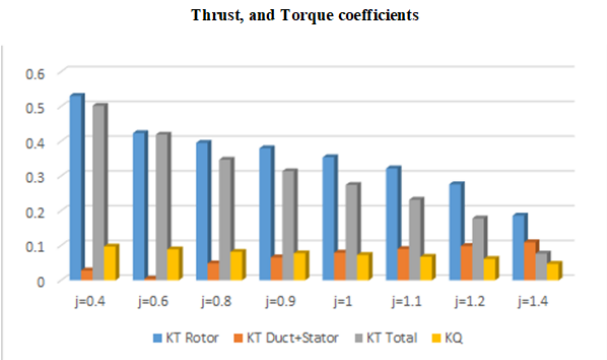


Fig. 18 Bar chart of rotor thrust coefficient, duct+stator thrust coefficient, total thrust coefficient, and torque coefficient obtained from experimental test results for L=0.050DR

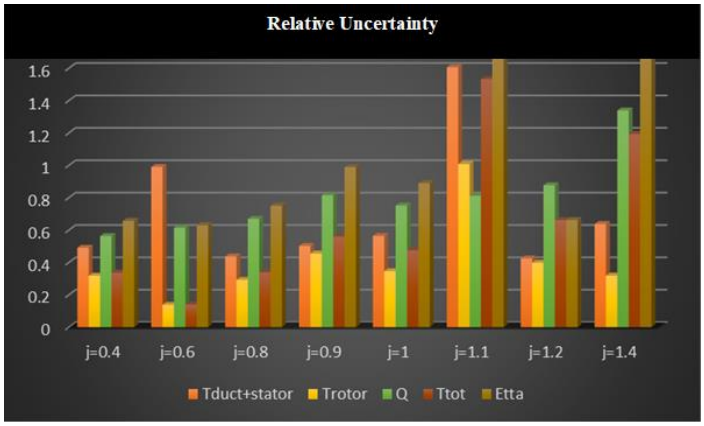


Fig. 19 Relative uncertainty values of duct-stator thrust, rotor thrust, total thrust, rotor torque, and open-water efficiency parameters as percentages at various advance ratios for L=0.050DR

9-4 Case 4: L=0.075DR

In this case, the inlet section length is considered to be 0.0675 meters. Based on the average of 4 sets of sampled thrust and torque values from the experimental test at different advance ratios, the maximum efficiency is 61.05% at an advance ratio of 1.1. The maximum thrust coefficient is 0.4761, and the maximum torque coefficient is 0.09353. In this case, similar to the previous cases, the open-water efficiency curve exhibits a completely ascending trend up to J=1.1, followed by a completely descending trend beyond this advance ratio. The thrust coefficient curve shows an approximately decreasing trend. The torque coefficient is similar to the previous case. Fig. 20 presents the efficiency, torque, and thrust coefficient values at various advance ratios. There is good agreement between the numerical and experimental results. Fig. 21 also shows the thrust and torque coefficients as bar charts, calculated using the average measured values of rotor thrust, duct-stator thrust, total thrust, and rotor torque. Fig. 22 presents the relative uncertainty values of duct-stator thrust, rotor thrust, total thrust, rotor torque, and open-water efficiency as percentages. As the graph shows, the maximum relative uncertainty occurs for open-water efficiency at 1.422993%, which is less than 5%, indicating the high accuracy of the experiments.

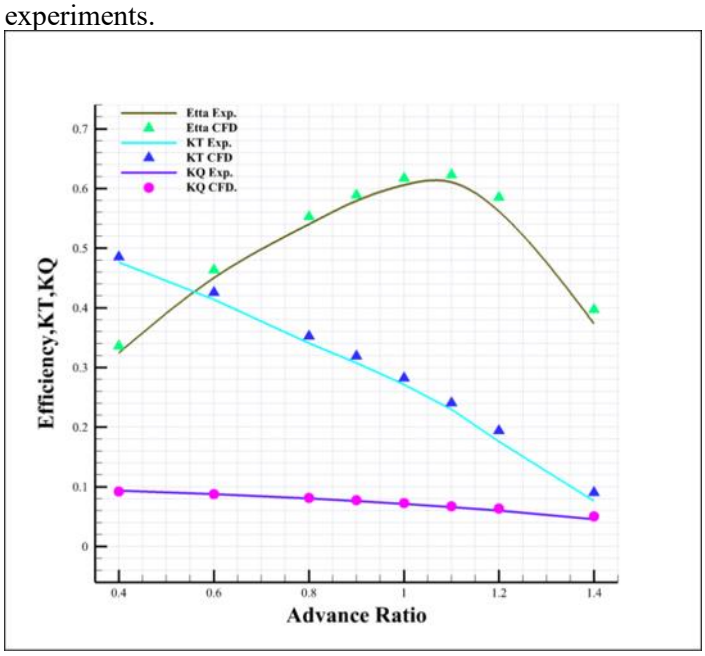


Fig. 20 Efficiency, thrust, and torque coefficients at various advance ratios for L=0.075DR

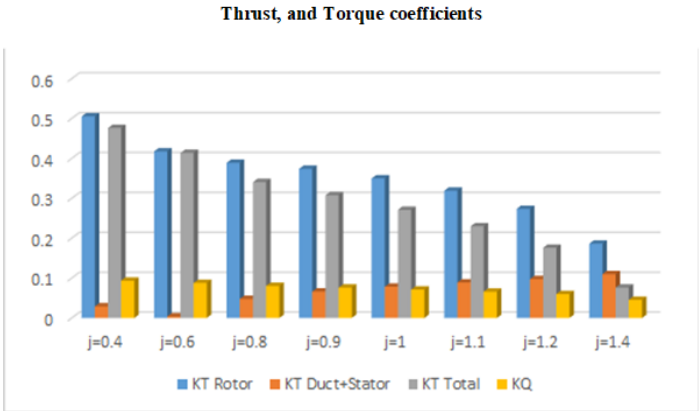


Fig. 21 Bar chart of rotor thrust coefficient, duct+stator thrust coefficient, total thrust coefficient, and torque coefficient obtained from experimental test results for L=0.075DR

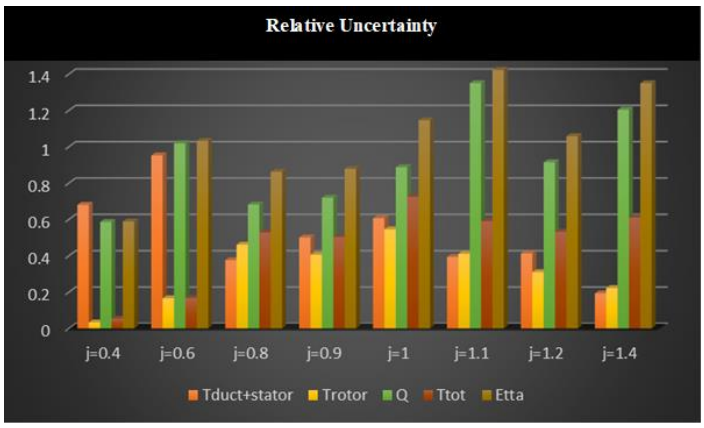


Fig. 22 Relative uncertainty values of duct-stator thrust, rotor thrust, total thrust, rotor torque, and open-water efficiency parameters as percentages at various advance ratios for L=0.075DR

9-5 Case 5: L=0.1DR

In this case, the inlet section length is considered to be 0.09 meters. Based on the average of 4 sets of sampled thrust and torque values from the experimental test at different advance ratios, the maximum efficiency is 62.15% at an advance ratio of 1.1. The maximum thrust coefficient is 0.5117, and the maximum torque coefficient is 0.0989. Similar to the previous cases, the open-water efficiency curve exhibits a completely ascending trend up to J=1.1, followed by a completely descending trend beyond this advance ratio. The maximum efficiency among all cases investigated is observed in this case. The thrust and torque coefficient curves also show a decreasing trend with an increasing advance ratio. Fig. 23 presents the efficiency, torque, and thrust coefficient values at various advance ratios. Fig. 24 also shows the thrust and torque coefficients as bar charts, calculated using the average measured values of rotor thrust, duct-stator thrust, total thrust, and rotor torque. Fig. 25 presents the relative uncertainty values of duct-stator thrust, rotor thrust, total thrust, rotor torque, and open-water efficiency as percentages. As the graph shows, the maximum relative uncertainty is for open-water efficiency at 1.663996%, which is less than 5%, indicating the high accuracy of the experiments.

Fig. 23 Efficiency, thrust, and torque coefficients at various advance ratios for L=0.1DR

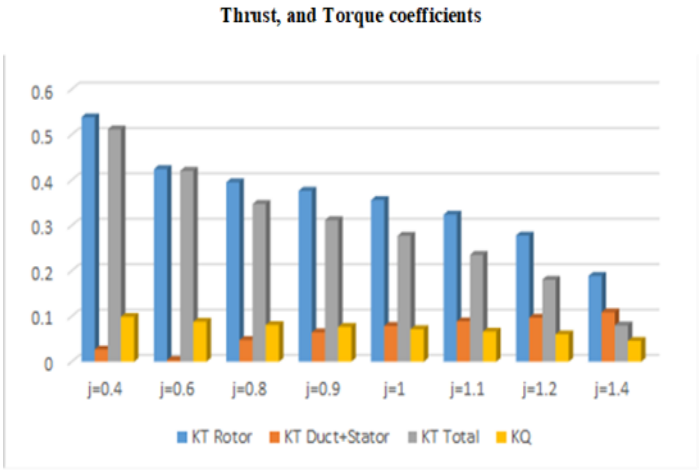
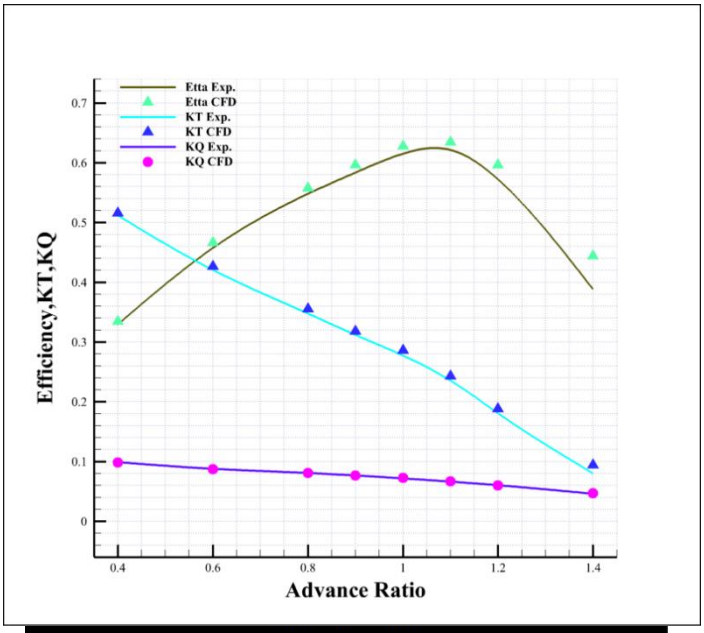


Fig. 24 Bar chart of rotor thrust coefficient, duct+stator thrust coefficient, total thrust coefficient, and torque coefficient obtained from experimental test results for L=0.1DR



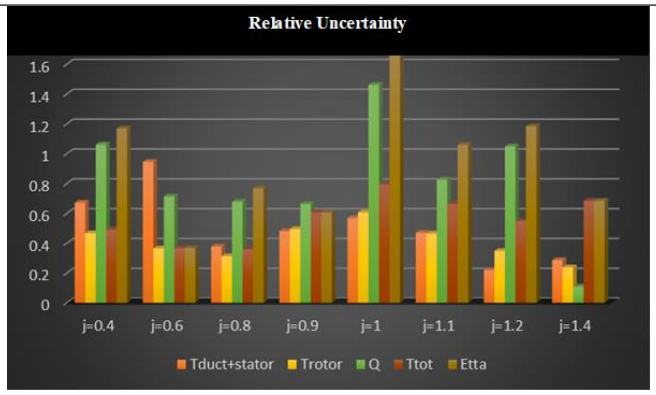


Fig. 25 Relative uncertainty values of duct-stator thrust, rotor thrust, total thrust, rotor torque, and open-water efficiency parameters as percentages at various advance ratios for L=0.1DR

10- RESULTS AND DISCUSSION

10-1 Pressure Coefficient Analysis

To analyze the pressure coefficient changes at different sections across the 0.7 span, for various advance ratios, measurements were taken. The positions of these sections are shown in Fig. 26. The results are presented in the graphs of Figs 27 and 28.

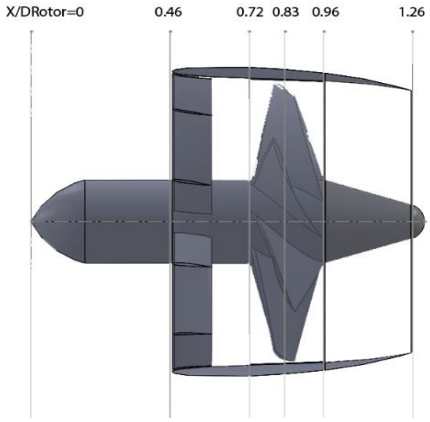


Fig. 26 Dimensionless section positions on the propeller.

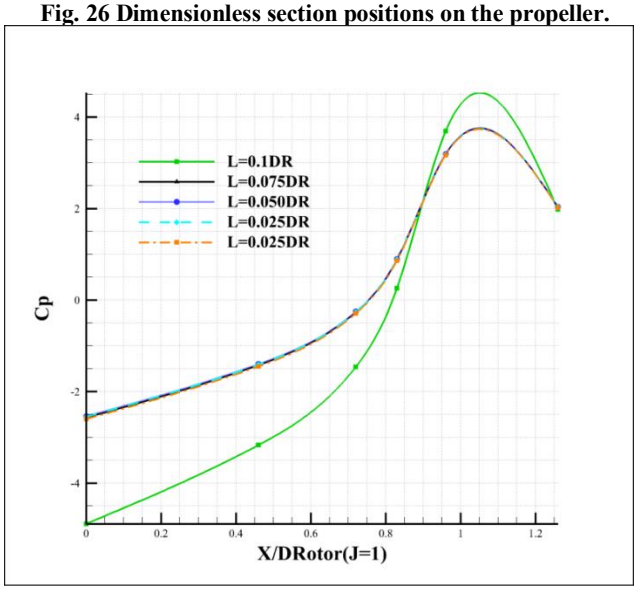


Fig. 27 Pressure coefficient variation plot across the propeller at an advance ratio of 1 (Numerical Simulation).

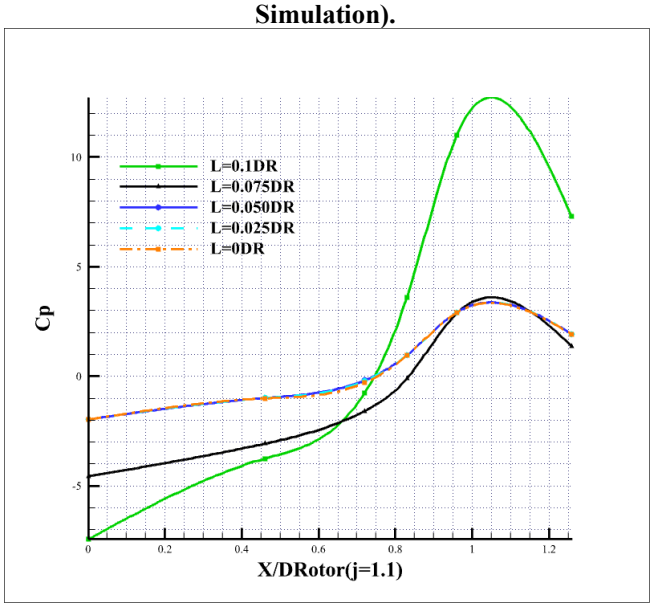
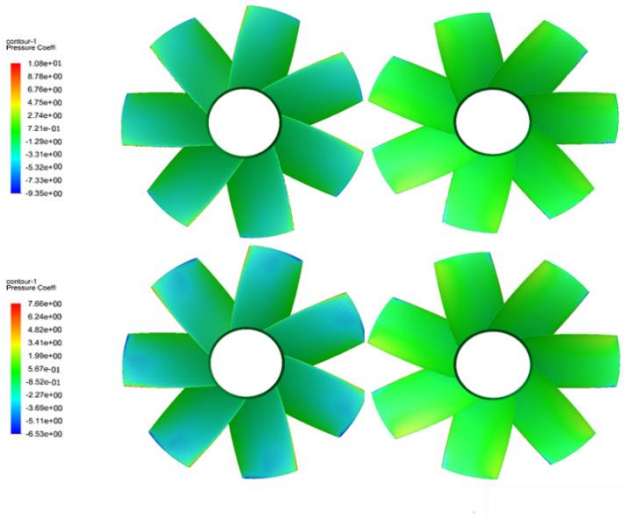


Fig. 28 Pressure coefficient variation plot across the propeller at an advance ratio of 1.1 (Numerical Simulation)

Examination of the pressure coefficient variation plots indicates a greater pressure difference across the rotor—as the primary thrust generator of the propeller—for the L=0.1DR case, which can lead to increased thrust and propeller efficiency. For the remaining four cases, the trends are more similar, and the values are close; however, in the L=0.1DR case, the pressure difference is higher. In the sections before the rotor inlet, the result is different, with the L=0.1DR case showing lower values compared to the other cases. Accordingly, moving the stator closer to the rotor will increase the pressure difference across the rotor, which holds the most advance ratios. The pressure coefficient contour at an advance ratio of 0.9 for the suction and pressure sides of the rotor for L=0.1DR and L=0DR cases are shown in Fig. 29. Examination of these contours also reveals a greater pressure difference



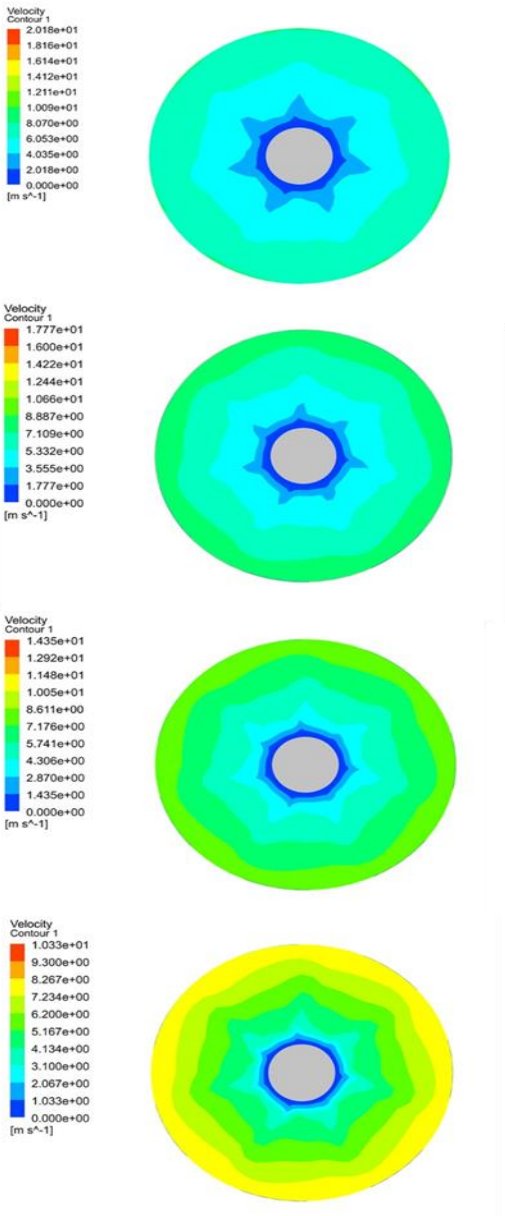
across the rotor for the L=0.1DR case.

Fig. 29 Pressure coefficient contour on the rotor, from left to right, suction and pressure sides, and from top to bottom, for L=0.1DR and L=0DR cases at an advance ratio of 1.1.

10-2 Velocity Analysis

After the pressure increases in the rotor and the flow exits it, it reaches the converging section of the duct, where the increased pressure converts to velocity, leading to an increase in momentum as the flow exits the duct. Fig. 30 shows the contour plots of flow velocity sections after passing the rotor at X/DRotor=1.1 at an advance ratio of 1.1. In the L=0.1DR case, high-velocity regions exist uniformly from span 0.65 onwards, and generally, from span 0.45 onwards, only two distinct velocity boundaries are discernible. In the velocity contour for the L=0.075DR case, three velocity boundaries are discernible from span 0.4 onwards, and the final high-velocity boundary

extends from span 0.8 to the end. In the L=0.050DR case, four-velocity boundaries are observable from span 0.35 onwards. The final high-velocity boundary is from span 0.8 to the end. In the L=0.025DR case, three boundaries are observable from span 0.35 onwards, and the final high-velocity boundary continues from span 0.8 to the end. On the L=0DR contour, four boundaries are discernible from span 0.35 onwards. The final high-velocity boundary is interdigitated with a lower velocity boundary from span 0.95 onwards. As observed, the velocity contour for the L=0.1DR case shows a higher velocity value compared to the other cases, in addition to having a more uniform velocity distribution, with similar conditions existing at other advance ratios. Fig. 31 also shows the velocity contour at different sections for the L=0DR case at an advance ratio of 0.9.



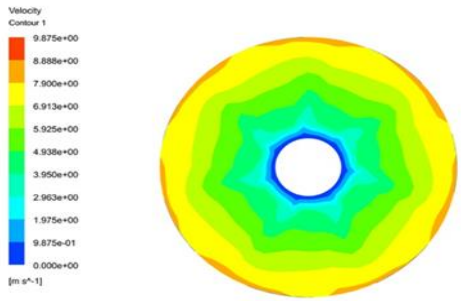


Fig. 30 Velocity contour at section X/DRotor=1.1, from up to down: L=0.1DR, L=0.075DR, L=0.050DR, L=0.25DR and L=0DR at an advance ratio of 1.1

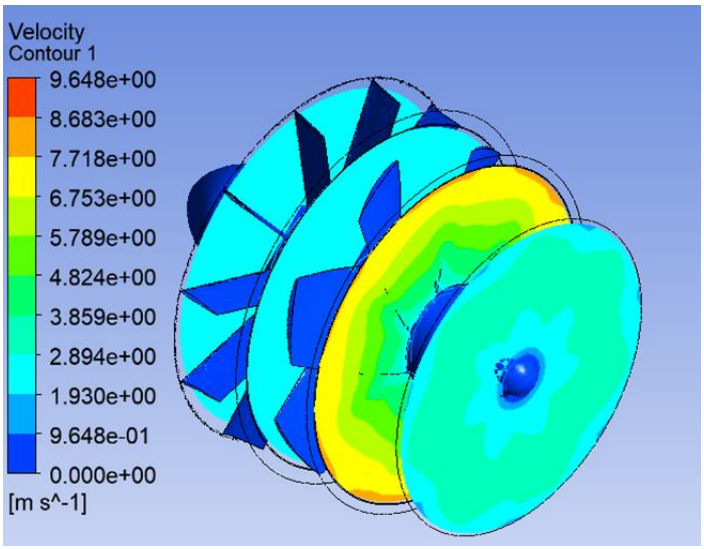


Fig. 31 Velocity contour at different sections for the L=0DR case at an advance ratio of 0.9.

Fig. 32 presents the contour of vortex core regions related to the axial velocity exiting the rotor using the Q-Criterion method for the L=0.1DR and L=0DR geometries at an advance ratio of 0.8. Examination of these two contours shows that at the rotor outlet for the L=0.1DR case, higher-speed vortices are formed from spin 0.7 onwards to the inner wall of the duct, indicating a higher flow velocity after passing the rotor and entering the converging section of the duct for the L=0.1DR case compared to L=0DR. Based on the analysis for the other cases as well, the axial velocity vortices exiting the L=0.1DR case have a higher value at most advance ratios.

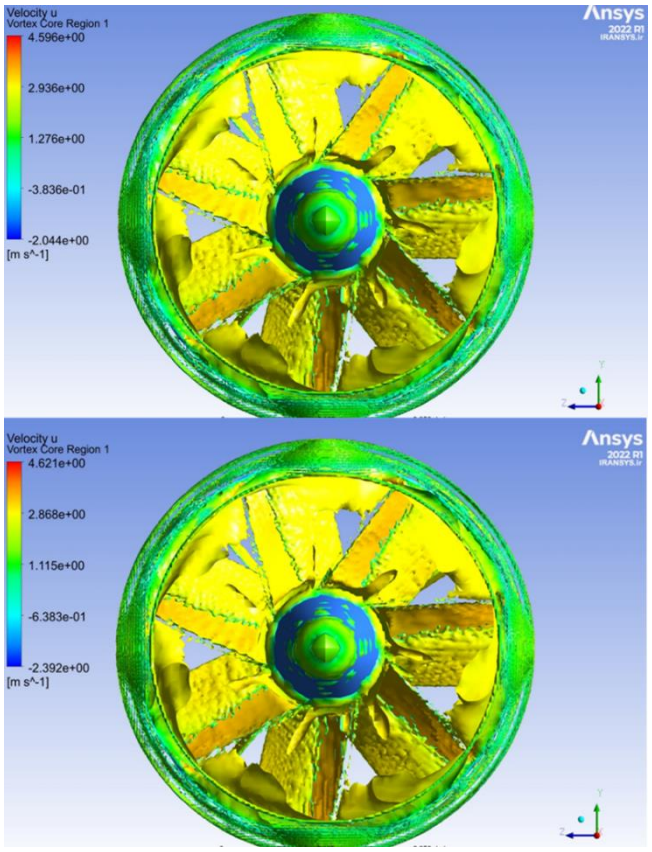


Fig. 32 Contour of vortex core regions related to the axial velocity exiting the rotor using the Q-Criterion method for the L=0.1DR and L=0DR geometries at an advance ratio of 0.8.

10-3 Streamline Analysis

Generally, for airfoil sections, with an increase in the angle of attack up to a specific range (often less than 20 degrees), the airfoil's lift coefficient increases. If, during this increase, the drag coefficient remains unchanged or decreases (the lift-to-drag ratio increases, or in the case of a propeller, thrust increases), the performance of the airfoil section improves. The streamlines for the L=0DR and L=0.1DR cases at an advance ratio of 1.1 are shown in Fig. 33. Their close examination reveals that as the stator blade approaches the rotor, more streamlines effect and exit the rotor blades at an appropriate angle of attack. The effect of streamlines at a suitable angle of attack (which should have been considered during stator design) will increase the rotor's hydrodynamic efficiency.

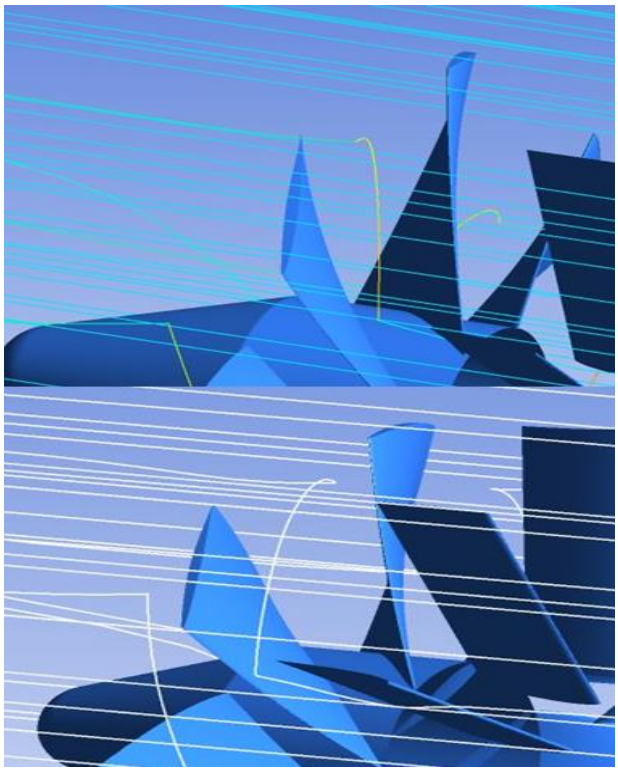


Fig. 33 Contour of streamlines passing from the stator to the rotor, from top to bottom, for L=0DR and L=0.1DR cases.

Fig. 34 also presents the rotor lift coefficient values for the five cases studied at advance ratios of 0.9, 1, 1.1, and 1.2. Examination of the values shows that as the stator approaches the rotor, the lift coefficient increases for most advance ratios, and there is a significant difference in the lift coefficient values for the L=0.1DR case compared to the other cases at advance ratios of 1 and 1.1.

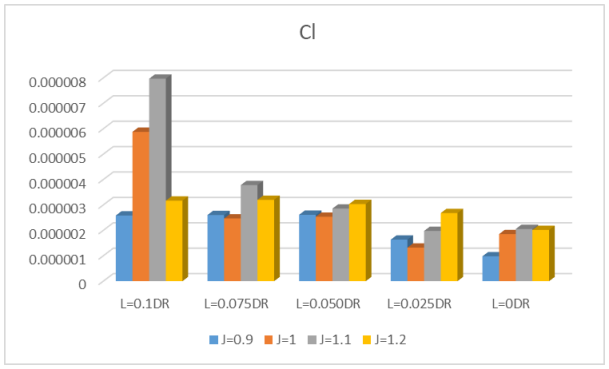


Fig. 34 Bar chart of rotor lift coefficient for the five cases studied at advance ratios of 0.9, 1, 1.1, and 1.2 (Numerical Simulation).

10-4 Total Thrust Coefficient

Based on the comparative graph in Fig. 36, the L=0.01DR case shows the highest total thrust coefficient among the different cases at all advance ratios. In the remaining cases, differences are observed in the ranges of J=0.4 to J=0.8 and J=1.1 to J=1.4, with no significant difference in other ranges. The trend for all cases is decreasing in the range of J=0.4 to J=0.6, increasing from J=0.6 to J=0.8, and then solely decreasing, except for the L=0.1DR case, which is increasing in the range of J=1.1 to J=1.4**.**

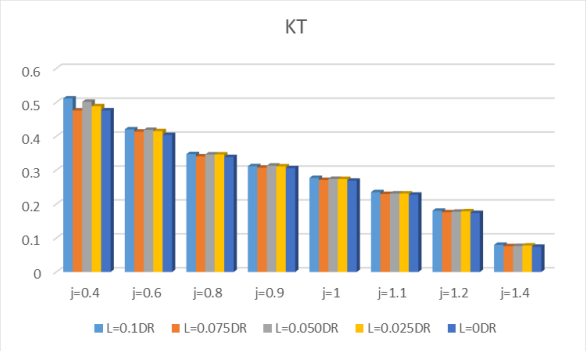


Fig. 35 Bar chart of total thrust coefficient for the five cases studied (Experimental Test).

10-5 Torque Coefficient

A careful examination of the graph in Fig. 37 shows that the L=0.025DR case has the highest torque coefficient of all advance ratios. In the other cases, there are also differences in the range of J=0.4 to J=0.6, and after this range, the values become similar. The trend for all cases is decreasing in the range of J = 0.4 to J = 0.6, approximately increasing from J = 0.6 to J = 0.8, and then decreasing again.

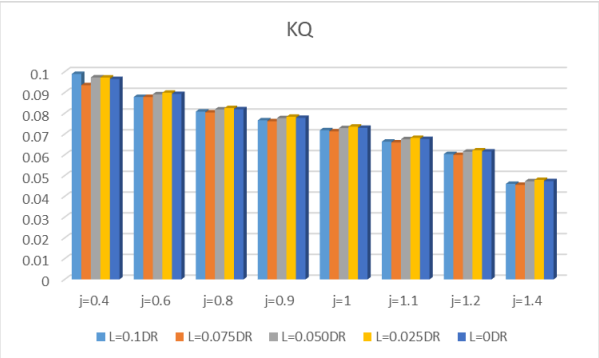


Fig. 36 Bar chart of torque coefficient for the five cases studied (Experimental Test).

As observed, the most significant fluctuations in both the thrust coefficient and the torque coefficient occur at lower advance ratios due to the influence of induced velocities from the stator on the rotor. On the other hand, with an increase in the duct inlet length, the proximity of the stator to the rotor, and the correct guidance of the flow at a higher angle of attack to the leading edge of the rotor, the fluctuations are reduced, and it is observed that these detrimental fluctuations are almost eliminated. The trend becomes uniform at higher advance ratios.

10-6 Open Water Efficiency

As evident from the comparative graph in Fig. 38, the propeller's open water efficiency increases with an increase in the duct inlet length and better and more accurate guidance of streamlines to the leading edges of the rotor blades (which, due to the arrangement of the stator blades, leads to an increase in the angle of attack of the flow to the rotor blades and, consequently, an increase in the rotor blades' lift coefficient). As observed, the L=0.1DR case has the maximum open water efficiency and, at most advance ratios except J=0.4, has higher efficiency than the others. The L=0.025DR case has the minimum efficiency at all advance ratios. The L=0.050DR, L=0.025DR, and L=0.075DR cases show a roughly similar trend and close values.

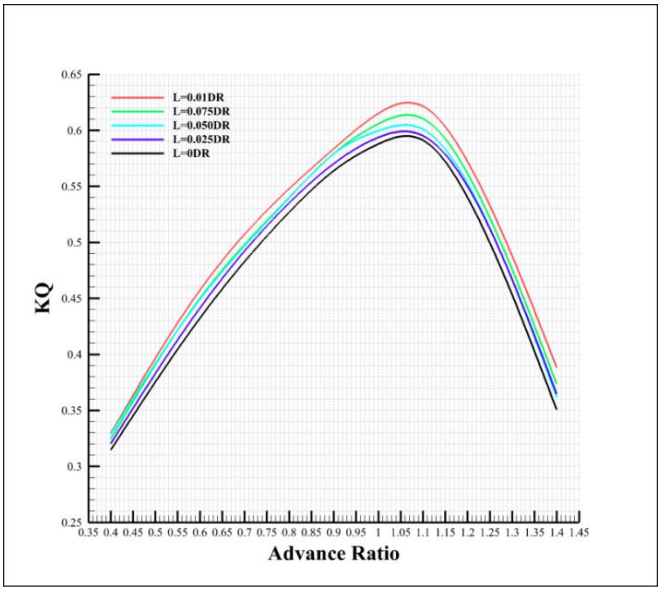


Fig. 37 Comparative graph of efficiency for the five inlet duct lengths studied at different advance ratios.

10-7 Relative Uncertainty

The relative uncertainty values for the duct and stator assembly thrust, rotor thrust, and total thrust are presented in Figs 13, 16, 19, 22, and 25. The relative uncertainty values for the duct and stator assembly thrust vary from 0.1001 (L=0DR, J=0.6) to 1.605497 (L=0.050DR, J=1.1). The relative uncertainty values for rotor thrust vary from 0.033333 (L=0.075DR, J=0.4) to 1.007751 (L=0.050DR, J=1.1). The relative uncertainty values for total thrust vary from 0.054456224 (L=0.075DR, J=0.4) to 1.533078 (L=0.050DR, J=1.1). The relative uncertainty values for rotor torque vary from 0.1087 (L=0.1DR, J=1.4) to 1.490312966 (L=0.025DR, J=1). The relative uncertainty values for open water efficiency vary from 0.368471123 (L=0.1DR, J=0.6) to 1.794043915 (L=0.050DR, J=1.4). Based on this, the maximum relative uncertainty among all these parameters is 1.794043915 (L=0.050DR, J=1.4), which is a desirable

value in engineering calculations and indicates the high accuracy of the experimental test conducted.

11- CONCLUSION AND SUMMARY

This study provides significant insights into the hydrodynamic performance of a pre-swirl pump-jet in open water by experimentally and numerically investigating the effects of duct inlet length and stator-rotor gap. Five configurations with varying duct inlet lengths (L/DR = 0, 0.025, 0.050, 0.075, 0.1) were studied both experimentally in a cavitation tunnel and through numerical simulations. The close agreement between experimental results and numerical simulations, performed using ANSYS Fluent software with the k-ω SST turbulence model and uncertainty analysis, confirms the reliability of the findings. The main research findings are as follows:

- Optimization of Duct Inlet Length and Stator-Rotor Distance: The results indicate that increasing the duct inlet length, accompanied by a reduced stator-rotor gap, leads to more appropriate guidance of the flow lines exiting the stator at a suitable angle of attack to the rotor blades. This increases the rotor lift coefficient and creates a greater pressure difference across the rotor. Upon entering the convergent section of the duct, this results in increased velocity and momentum, ultimately leading to an increase in the total thrust coefficient of the propulsor and a subsequent significant increase in open-water efficiency. The configuration with L=0.1DR achieved the highest efficiency of 62.15% at an advance ratio of 1.1, which was 5% higher than the lowest efficiency (59.12%) of the L=0DR case at the same advance ratio. In most other advance ratios, the L=0.1DR case also exhibited the maximum open-water efficiency.
- Performance Criteria and Uncertainty Analysis: The performance of the pump-jet propulsor is evaluated based on efficiency, thrust coefficient, and torque coefficient in open-water conditions. The calculated relative uncertainty values were all less than 5%, indicating the accuracy of the experiments conducted.
- Comparison of Configurations: This study compares the pump-jet performance under various configurations. The results show that the configuration with L=0.1 DR is preferred over the others due to its more favorable hydrodynamic performance. This configuration demonstrated more uniform flow, a greater pressure difference across the rotor, and stable performance over a broader range of advance ratios.
- Performance Improvement: The improved performance is attributed to better guidance of flow lines from the stator to the rotor, an increased rotor lift coefficient, a larger pressure difference across the rotor, and a greater increase in axial velocity after the flow enters the convergent section of the duct.
- Scientific and Practical Implications: The findings of this research have significant implications for the design of marine propulsion systems, especially for underwater vehicles such as submarines and autonomous underwater vehicles (AUVs). Optimizing the duct inlet length and stator-rotor gap can enhance hydrodynamic efficiency, which is crucial for extended operational range. These improvements reduce energy consumption, aligning with global sustainability goals. The principles presented in this study can also be applied to the design of other fluid machinery, such as hydroelectric turbines or ducted fans. The combined experimental and numerical methodology, including rigorous cavitation tunnel tests and high-fidelity CFD simulations with uncertainty analysis, provides a reliable framework for future research in hydrodynamics.
- Limitations and Future Research Directions: Despite the advancements made, this study has limitations that highlight the need for further investigation in the future. The experiments were conducted in a controlled cavitation tunnel environment, which may not fully simulate real-world effects such as wall effects, vortex integration effects in the wake region, or variable marine conditions. Future research should investigate these parameters under actual operating conditions, taking into account wall effects and varying flow regimes. Additionally, studying noise generation and cavitation inception, which are crucial for stealth applications and system durability, is essential. Investigating scale effects (model vs. full-scale) can help identify more optimal configurations.
- Final Summary: This study advanced the understanding of pre-swirl pump-jet hydrodynamics by providing a comprehensive analysis of the effect of duct inlet length and stator-rotor gap. The optimal configuration (L = 0.1 DR) offered significant efficiency, providing practical guidelines for designing more efficient and sustainable propulsion systems. These findings contribute to the advancement of marine technology by filling the stated gap in research, paving the way for the development of underwater vehicles with superior performance. Future research on noise, cavitation, and real-world conditions will extend the practical effect of these findings, solidifying the pump jet as a cornerstone of future underwater marine propulsion.

REFERENCES

[1] Bertram, V. (2012). Practical ship hydrodynamics. Oxford, U.K, Butterworth Heinemann.

[2] Bi, Z., Zhang, L., Shao, X., & Bao, F. (2023). Numerical study of two types of rough groove in suppressing the tip clearance cavitation. International Journal of Multiphase Flow, 168, 104564. https://doi.org/10.1016/j.ijmultiphaseflow.2023.104564

[3] Carlton, J. S. (2012). Marine propellers and propulsion (3rd ed.). Amsterdam, Netherland, Elsevier.
[4] Chen, X., Cheng, L., Wang, C., & Luo, C. (2021). Influence of inlet duct length on the hydraulic performance of the waterjet propulsion device. Shock and Vibration, 2021(1), 6676601. https://doi.org/10.1155/2021/6676601
[5] Coleman, H. W., & Steele, W. G. (1999). Experimentation and Uncertainty Analysis for Engineers. John Wiley and Sons, Inc., New York.
[6] Dean, A., & Voss, D. (1999). Design and Analysis of Experiments. Springer Verlag, New York.
[7] Huang, Q., Li, H., Pan, G., & Dong, X. (2021). Effects of duct parameter on pump-jet propulsor unsteady hydrodynamic performance. Ocean Engineering, 221, 108509. https://doi.org/10.1016/j.oceaneng.2020.108509
[8] Huang, Q., Qin, D., & Pan, G. (2022). Numerical simulation of the wake dynamics of the pumpjet propulsor in oblique inflow. Physics of Fluids, 34(6). https://doi.org/10.1063/5.0091408
[9] Ji, X. Q., Zhang, X. S., Yang, C. J., & Dong, X. Q. (2024). Experimental and numerical investigation of the effects of rotor tip-rake on excitation forces of pump-jet propulsors. Journal of Hydrodynamics, 1-16. https://doi.org/10.1007/s42241-024-0011-0
[10] Kim, J.-W., Kim, M.-C., Park, I.-R., Seol, H., Kim, M.-J., & Jin, W.-S. (2023). Parametric Study of the Hydrodynamic Characteristics of the Pumpjet Propulsor for the SUBOFF Submarine. Journal of Marine Science and Engineering, 11(10), 1926. https://doi.org/10.3390/jmse11101926
[11] Li, H., Huang, Q., & Pan, G. (2022). Investigation on the Propulsion of a Pump-Jet Propulsor in an Effective Wake. Journal of Fluids Engineering, 144(5).
[12] Li, X. R., Ding, Y., & Wang, W. Q. (2022). The hydrodynamic performance analysis of a submarine with new pump-jet propulsor. Ocean Engineering, 245, 110542.
[13] Lidtke, A. K., Lloyd, T., Lafeber, F. H., & Bosschers, J. (2022). Predicting cavitating propeller noise in off-design conditions using scale-resolving CFD simulations. Ocean Engineering, 254, 111176. https://doi.org/10.1016/j.oceaneng.2022.111176
[14] Morrison, A. (2018). A comparison of pump jets and propellers for non-nuclear submarine propulsion.
[15] Motallebi-Nejad, M., Bakhtiari, M., Ghassemi, H., & Fadavie, M. (2017). Numerical analysis of ducted propeller and pumpjet propulsion system using periodic computational domain. Journal of Marine Science and Technology, 22, 559–573. https://doi.org/10.1007/s00773-017-0438-x
[16] Nakra, B. C., & Chaudhry, K. K. (2016). Instrumentation Measurement and Analysis (4th ed.).
[17] Qaedsharaf, M. H. (2011). Analysis of heat transfer and fuel regression rate of solid fuel in hybrid thrusters [M.Sc. Thesis]. Islamic Azad University, Science & Research Branch.
[18] Qaedsharaf, M. H., Mahdavi, H., & Mehrabi Gohari, E. (2019). Comparison of performance and sensitivity of effective parameters in two propellants hydrogen peroxide and nitrous oxide using uncertainty analysis. Mechanical Engineering, University of Tabriz, 50(3), 233-237. https://doi.org/10.22034/JMEUT.2020.9802
[19] Qaedsharaf, M. H., Yari, E., & Manshadi, M. D. (2025). Cavitation on the pump jet pre swirl type due to changes in the stator chord length. Physics of Fluids, 37(3). https://doi.org/10.1063/5.0248017
[20] Qin, D., Huang, Q., Pan, G., Shi, Y., Han, P., & Dong, X. (2021). Comparison of hydrodynamic performance and wake vortices of two typical types of pumpjet propulsor. Ocean Engineering, 224, 108700. https://doi.org/10.1016/j.oceaneng.2021.108700
[21] Qiu, C., Huang, Q., & Pan, G. (2022). Prediction of Cavitation Performance over the Pump-Jet Propulsor Using Computational Fluid Dynamics and Hybrid Deep Learning Method. Journal of Marine Science and Engineering, 10(7), 918. https://doi.org/10.3390/jmse10070918
[22] Qiu, C., Huang, Q., Pan, G., Shi, Y., & Dong, X. (2020). Numerical simulation of hydrodynamic and cavitation performance of pumpjet propulsor with different tip clearances in oblique flow. Ocean Engineering, 209, 107285. https://doi.org/10.1016/J.OCEANENG.2020.107285
[23] Renilson, M. R. (2018). Submarine hydrodynamics (2nd ed.). Springer, Cham. https://doi.org/10.1007/978-3-319-79057-2
[24] Sun, Y., Peng, H., Liu, W., Guo, J., & Guo, Y. (2022). Comparison of the hydrodynamic performance of front and rear-stator pump-jet propulsors in an oblique wake under the cavitation condition. Physics of Fluids, 34(3). https://doi.org/10.1063/5.0082769
[25] Suryanarayana, C., Rao, M. N., Raju, P. N., Balakrishan, T., & Lambada, S. (2012). Torque Balance and Cavitation Studies on Underwater Vehicle Propulsion System. International Journal of Innovative Research and Development, 1, 62-73.
[26] Wang, C., Weng, K., Guo, C., Chang, X., & Gu, L. (2020). Analysis of influence of duct geometrical parameters on pump jet propulsor hydrodynamic performance. Journal of Marine Science and Technology, 25, 640–657. https://doi.org/10.1007/S00773-019-00662-Z
[27] Weng, K., Sun, C., Han, K., Wang, C., Sun, S., Li, P., & Hu, J. (2024). Experimental/numerical investigation on the hydrodynamic and noise characteristics of pump-jet propulsion. Ocean Engineering, 307, 117995. https://doi.org/10.1016/j.oceaneng.2024.117995
[28] Yang, J., Feng, D., Liu, L., Wang, X., & Yao, C. (2022). Research on the Performance of Pumpjet Propulsor of Different Scales. Journal of Marine Science and Engineering, 10(1), 78. https://doi.org/10.3390/jmse10010078
[29] Ye, J. M., Sun, D. P., Zou, X. Y., Wu, Y. R., & Xi, P. (2022). Tip flow control performance and mechanism of axial slots in a pumpjet propulsor. Ocean Engineering, 266, 112950. https://doi.org/10.1016/j.oceaneng.2022.112950
[30] Zhao, X., Zhang, D., Shen, X., Geng, L., & van Esch, B. B. (2022). Numerical investigation on cavitation-vortex interaction in a scaled pre-swirl pump-jet propulsor.
[31] Zhou, Y., Pavesi, G., Yuan, J., & Fu, Y. (2022). A Review on Hydrodynamic Performance and Design of Pump-Jet: Advances, Challenges and Prospects. Journal of Marine Science and Engineering, 10(10), 1514. https://doi.org/10.3390/jmse10101514
[32] Zhou, Y., Pavesi, G., Yuan, J., Fu, Y., & Gao, Q. (2023). Effects of duct profile parameters on flow characteristics of pump-jet: A numerical analysis on accelerating and decelerating ducts distinguished by cambers and angles of attack. Ocean Engineering, 281, 114733. https://doi.org/10.1016/j.oceaneng.2023.114733

[33] Zou, D., Xue, L., Lin, Q., Xu, J., Dong, X., Ta, N., & Rao, Z. (2024). Influence of propulsion shafting longitudinal vibration on the excitation force and vortex dynamics characteristics of pump-jet propulsor. Ocean Engineering, 295, 116962. https://doi.org/10.1016/j.oceaneng.2024.116962.